Green's function technique for studying electron flow in two-dimensional mesoscopic samples

G. Metalidis* and P. Bruno†
Max-Planck-Institut für Mikrostrukturphysik, Weinberg 2, D-06120 Halle, Germany‡
(Received 29 November 2004; revised manuscript received 19 October 2005; published 2 December 2005)

With scanning probe experiments, it became possible to visualize electron flow in a two-dimensional electron gas. In this paper, a Green's function technique for efficient simulation of such experiments is presented. Interpretation of the experiments is further facilitated by a calculation of the current distribution. Furthermore, an alternative imaging method is put forward for measuring the local chemical potential. As an application, electron flow through a quantum point contact is studied. All features seen in experiments are reproduced, and an interference effect is predicted resulting from the crossing of coherent beams of electron flow.

DOI: 10.1103/PhysRevB.72.235304 PACS number(s): 73.23.−b, 73.63.−b, 73.43.Cd

I. INTRODUCTION

Electronic transport properties in mesoscopic systems have gained a lot of attention in the last two decades (for a review see, e.g., Refs. 1 and 2). A lot of effort already went into the study of global transport quantities (mainly conductance), and a range of interesting phenomena emerged: e.g., quantized conductance in a point contact,[3] the quantum Hall effect,[4] and universal conductance fluctuations[5] to name a few.

Recently, scanning probe methodshave offered the possibility of obtaining local information on electron transport, not accessible with ordinary global measurements, by using a scanning tunneling microscope tip as a localized scatterer and measuring the conductance change of the sample as a function of the tip position. This makes it possible to obtain a spatial map of electron flow in a two-dimensional electron gas (2DEG).[6–8] Such visualizations of current flow are interesting both from an experimental and a theoretical point of view.

The results obtained in these experiments were mainly interpreted with the help of electron or flux density calculations. Here, a numerical technique is developed that allows us to calculate in an efficient way the quantity that is actually measured, which is a conductance difference as a function of the tip position. The standard recursive Green's function (SRGF) method used in Ref. 9 is not very efficient because one has to start over the complete calculation for every tip position. The numerical effort then scales like M^4N^2 in the number of operations, where M is the width and N is the length of the system ($N \gg 1$), and one therefore is limited to small systems. On the other hand, our method scales like M^3N for the same problem. Moreover, with our method it is straightforward to obtain other relevant information like the local density of states and the electron and current density distributions which can then be compared with the experimental observables. These quantities are unavailable with the standard technique.

The imaging technique with the tip as a scatterer will not always give the expected results in the regime of high magnetic fields. To obtain more information about electron flow in this regime, a measuring method is proposed where the STM tip is used as a local voltage probe.

The paper is subdivided as follows: In Sec. II, the imaging method used in Refs. 6 and 7 is briefly reviewed and the voltage probe method is described. In Sec. III, we discuss how the considered systems can be described within a tight-binding model. Our numerical method is then applied to study electron flow through a quantum point contact in Sec. IV, while technical details of the method are discussed in Sec. V and in the appendixes.

II. IMAGING METHODS

A. Tip as a local scatterer

The experiments in Refs. 6 and 7 take place as follows: Current is passed via two contacts through a 2DEG, while simultaneously a scanning probe tip is moved across the sample. The local electrostatic potential that results from a negative voltage on the tip can function as a scattering center for electrons in the device. If the tip is placed over a region where a lot of electrons are flowing, the conductance of the sample will decrease considerably because of enhanced backscattering due to the tip, whereas in an area of low electron flow, the conductance decrease will be small. As such, by mapping the conductance decrease of the sample to the tip position, one gets a spatial profile of electron flow.

The relevant quantity for this imaging method is the position-dependent conductance difference

$$\Delta g(x,y) = g_0 - g_t(x,y), \tag{1}$$

where $g_t(x,y)$ is the conductance with the tip positioned on a point (x,y) and g_0 is the conductance without the tip. Conductances can be calculated within the Landauer-Büttiker formalism

$$g = \frac{2e^2}{h}T, \tag{2}$$

where T is the transmission coefficient between the contacts. Since g is a two-terminal conductance, it is symmetric with respect to reversal of the direction of an applied magnetic field: $g(+\mathbf{B}) = g(-\mathbf{B})$,[10] and therefore the map of electron flow obtained with this scattering method has the same symmetry.

B. Tip as a voltage probe

The imaging method in the previous section can give nice visualizations of the electron flow, as proven by the experimental results of electron transport through a quantum point contact.[6,7] One of the interesting subjects to study with this imaging method would be the quantum Hall effect, because, even after intensive theoretical and experimental effort, since its discovery[4] some of the details of electron transport in this regime remain unclear. Unfortunately, the appearance of edge states in the high-field regime leads to the suppression of backscattering,[11] so that the method described above will not yield the expected results in the quantum Hall limit.

However, a picture of this edge-state transport can be obtained by investigating the local chemical potential in the sample. This can be done using the STM tip as a voltage probe; the STM tip voltage equilibrates itself to the local chemical potential when electrons are allowed to tunnel into and out of the tip. Experimentally, this technique has already been used to probe the potential distribution at metal-insulator-metal interfaces[12] and at grain boundaries.[13]

In this case one has three contacts: the left and right contact through which a current is passed and the STM tip that measures a voltage. For this three-lead structure, one obtains for the voltage on the tip[1]

$$V_{\mathrm{tip}} - V_L = \frac{T_{\mathrm{tip},L}}{T_{\mathrm{tip},L} + T_{\mathrm{tip},R}}(V_R - V_L), \tag{3}$$

with V_p the voltage on lead p.

This imaging mode corresponds to making a three-terminal measurement, which means that the obtained spatial map will not be invariant under magnetic field reversal. The only symmetry relations that hold are $T_{pq}(+\mathbf{B}) = T_{qp}(-\mathbf{B})$,[10] so the information obtained when the tip is used as a voltage probe is different from that when the tip is used as a local scatterer, and both imaging methods will contribute differently to our understanding of electron flow in two-dimensional (2D) systems.

C. Charge and current density

One can (at least in principal) experimentally observe the total current density in the sample by measuring the magnetic field it induces. Another physically observable quantity is the total charge density, due to the electrostatic field it generates. Both of these quantities can also be calculated within the numerical framework presented in Sec. V and Appendices A and B.

Since we have access to the electron density, it would also be possible to include self-consistently the effect of the applied voltage and the resultant current flow on the transport properties. However, this will not be pursued further in this paper.

III. SYSTEM MODELING

The system we will consider is a two-dimensional device connected to semiinfinite leads extending in the x direction. By discretizing the Schrödinger equation, one obtains the standard tight-binding model

$$H = \sum_{n=-\infty}^{\infty}\sum_{m=1}^{M} \epsilon_{mn}|m,n\rangle\langle m,n| + \sum_{n=-\infty}^{\infty}\sum_{m=1}^{M-1} (t^x_{m,n}|m,n+1\rangle \times\langle m,n| + t^y_{m,n}|m+1,n\rangle\langle m,n| + \mathrm{H.c.}), \tag{4}$$

where (m,n) label the sites on the lattice, and ϵ_{mn} are the on-site energies. Sites are not meant to represent atoms as in the usual tight-binding model; rather they may represent a region containing many atoms, but this region should be small with respect to physically relevant quantities such as the Fermi wavelength. The quantities $t^x_{m,n}$ ($t^y_{m,n}$) give the hopping amplitude in the horizontal (vertical) direction. Since a square lattice is assumed, one has (in absence of magnetic fields)

$$t^x_{m,n} = t^y_{m,n} = -t = -\frac{\hbar^2}{2m^* a^2}, \tag{5}$$

with a the lattice spacing, and m^* the effective mass of the electron.

The leads extend from $n=-\infty,\cdots,0$ for the left lead, and $n=N+1,\cdots,\infty$ for the right one. The device itself is comprised by the other $M\times N$ sites. In the leads, only homogeneous fields perpendicular to the 2D device will be considered, while both homogeneous and inhomogeneous fields can be treated in the central device. The fields are described by Peierls substitution[14]

$$t^{x(y)}_{mn} = -te^{-\mathrm{i}e/\hbar\int \mathbf{A}\cdot d\mathbf{l}}, \tag{6}$$

where $\int \mathbf{A}\cdot d\mathbf{l}$ is the integral of the vector potential along the hopping path.

IV. APPLICATIONS

In the preceding section, we have discussed quite a lot of quantities giving information about the flow of electrons in a 2DEG. Before giving explicit technical details about our numerical method, we will first show calculation results for two physical systems.

A. Single quantum point contact

The first system that we consider is the one that is used in the experiment of Topinka *et al.*[7] It consists of a 2DEG with a quantum point contact in the middle. The point contact is modeled by a potential of the form

$$W\exp^{-x^2/\xi^2}y^2. \tag{7}$$

We have taken a lattice of 1001 by 351 sites, with a lattice parameter of $a=6.2$ nm, which corresponds to a hopping parameter $t=14.5$ meV (the effective mass of the electron is taken to be that for electrons in GaAs: $m^\star=0.068m$). The parameters of the potential are chosen as $W=0.56t$ and $\xi=10a$. The Fermi energy is put equal to $E_F=1.1t=16$ meV (corresponding to a wavelength $\lambda_F=6a$), which is on the first conductance plateau of the point contact. For the calculations where the tip is used as a local scatterer, the strength of the delta function scattering potential used to model the tip is chosen to be $v=8t$. Disorder in the system is modeled by a

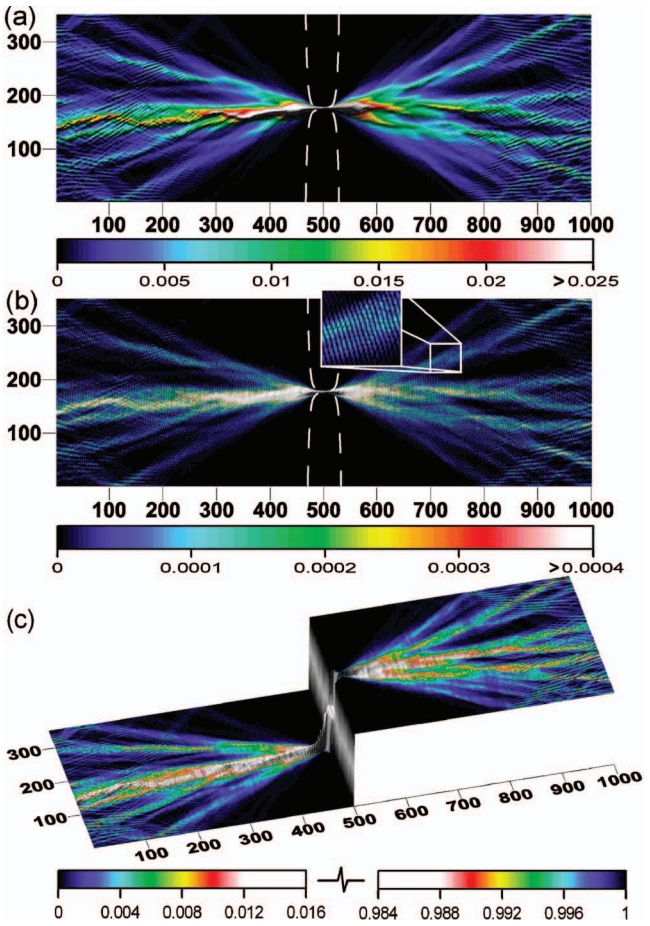

FIG. 1. (Color) Maps of electron flow through a quantum point contact. Lengths on the axes are given in units of the lattice parameter a. Current density distribution (a) in units of $2e^2V/(ha)$, STM conductance map (b) (conductance is measured in units of $2e^2/h$), and STM volt probe map (c). The voltage on the left lead $V_L=0$ and voltage is measured in units of V_R. The Fermi energy contour is depicted as a dotted white line. There is a clear correspondence between the different images.

plane of impurities above the 2DEG, where the repulsive potential from a single impurity is taken to vary with distance r as $1/r^3$, which is characteristic for the screened potential in a 2DEG from a point charge.[15] The concentration of impurities is fixed at 1% of the total number of lattice sites. The impurity lattice is located at a distance $6a$ above the 2DEG. Within the Born approximation, the mean free path of the potential we use is estimated to have a value of 4×10^3a which is much longer than the system size so that we are in the ballistic regime. The mobility corresponding to these parameters is of the order $\mu\approx2\times10^6$ cm^2/V s.

In Fig. 1(a), the calculated current density is seen to exhibit a branching behavior that was also apparent in the experiment in Ref. 7. The branched flow is also present in the map of the conductance difference versus the tip position, when the tip is used as a local scatterer [Fig. 1(b)]. It is clear that there is a direct correspondence between the current density calculation and the conductance map. Therefore one can conclude that the experiment in Refs. 6 and 7 really probes the current distribution in the sample. Also visible in the conductance difference map are the interference fringes spaced by half the Fermi wavelength [see the inset in Fig. 1(b)], which were explained as resulting from scattering between the point contact and the STM tip.[6] The magnitude of the conductance decrease in our calculations is smaller than in the experiment, because we model the tip as a delta function while it has a finite width in the experiment, thus scattering electrons more effectively. The map of the local chemical potential, as measured by the STM voltage probe [Fig. 1(c)] in this case gives similar information as the previous plots: On the left the current flow appears as regions with increased voltage compared to that of the left lead (V_L is put equal to zero). This corresponds to a decreased chemical potential due to a deficit of electrons resulting from the nonequilibrium transport process. On the right, the current flow appears as regions with a decreased voltage compared to the right lead. This corresponds to an increased chemical potential (excess electrons due to the transport process).

Small oscillations of the chemical potential with a wavelength on the order of $\lambda_F/2$ are apparent in Fig. 1(c). They result from interference between paths which emerge from the leads and directly enter the probe, and paths which first pass the probe, are reflected from the quantum point contact (QPC) and only then enter the probe. This effect was already described in Ref. 16: The voltage measurement we make is phase sensitive.

In Fig. 2, the quantities are calculated for the same system as before, but now a magnetic field is included. The field is characterized by a magnetic length of $l_B=28a$ and a cyclotron radius $r_c=835a$. From the nonequilibrium transport current density plot [which is symmetric in the magnetic field by its definition in Eqs. (22a) and (22b)], it is clear that the branches of electron flow start bending. The radius of curvature has the same order of magnitude as the cyclotron radius, so we are seeing here the onset of the skipping orbit movement of the electrons. The branches are reflected on the upper and lower edges of the sample, proof that one is still in the ballistic regime.

The conductance difference map [Fig. 2(b)] is quite unclear. This can be explained as resulting from the reduction of backscattering in the presence of a magnetic field.[11] But nevertheless, the tendency of the branches to curve can be observed.

In this regime, the voltage probe method gives better results. The curved branches are clearly visible in Fig. 2(c). Please keep in mind that the voltage method is not symmetric under reversal of the field, which results in the asymmetry of the voltage map. This asymmetry will be explained in more detail with the help of Fig. 3(c).

In Fig. 3, results are shown for a high magnetic field (magnetic length $l_B=4.8a$, cyclotron radius $r_C=24a$). In a plot of the transport current density the electrons are seen to describe skipping orbits along the edges of the sample; we are in the quantum Hall regime. In this regime the original tip scattering method fails because of a lack of backscattering.[11] This is visible in Fig. 3(b) only in the middle of the quantum point contact there is some conductance decrease because in this region waves traveling in opposite directions are "forced" to overlap. The map of the local chemical potential [Fig. 3(c)] gives better results: the skipping orbits are clearly visible.

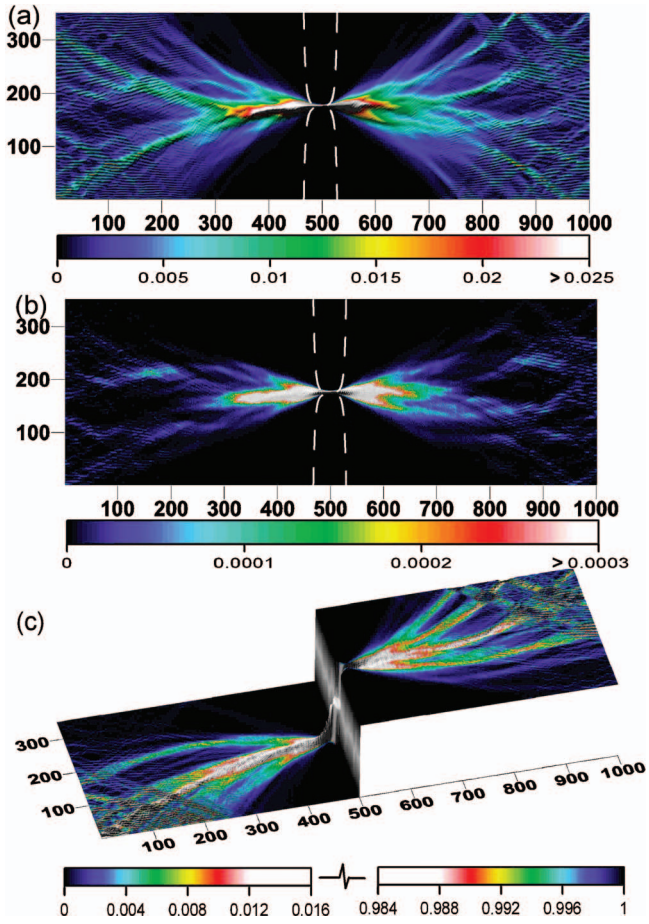

FIG. 2. (Color) Maps of electron flow through a quantum point contact with a moderate magnetic field. Transport current density distribution (a), STM conductance map (b) and STM volt probe map (c). Units on the color scales are the same as in Fig. 1.

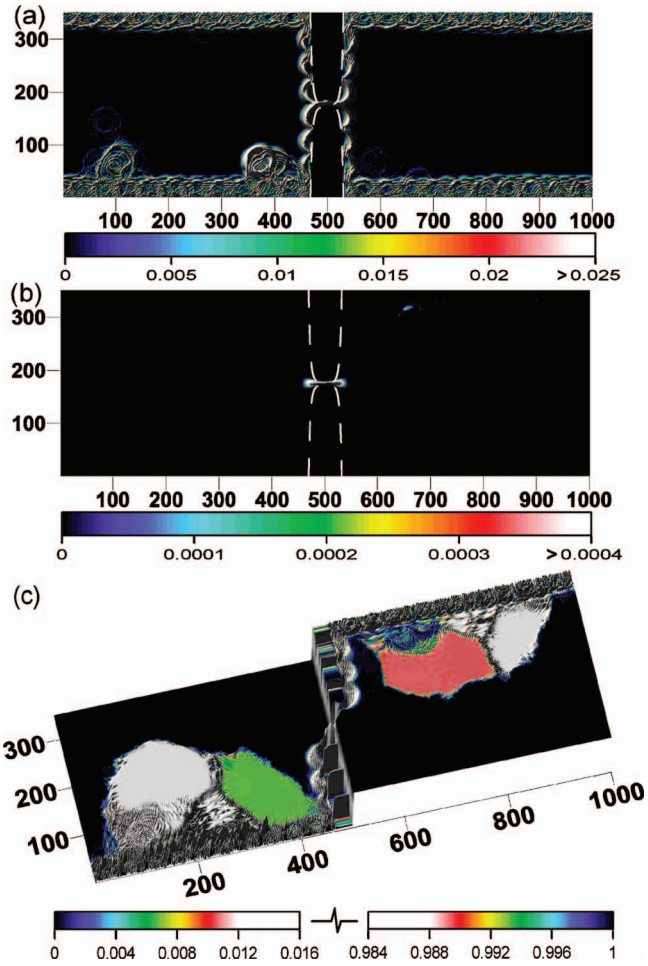

FIG. 3. (Color) Maps of electron flow through a quantum point contact with a high magnetic field. Transport current density distribution (a), STM conductance map (b), and STM volt probe map (c). Units on the color scales are the same as in Fig. 1.

The asymmetry of this plot was already pointed out above, and can be understood as follows: the voltage on the right lead is chosen to be higher than that on the left lead, so electrons are flowing from the left to the right. The magnetic field for this plot is pointing out of the plane of the paper, so electrons emerging from the left lead flow along the upper left edge of the sample, and this edge is in equilibrium with the left lead (no skipping orbits are seen on this edge, only a uniform potential distribution). Some of these electrons are transmitted through the point contact, which results in a higher chemical potential (so there is lower voltage) than μ_R at the upper right edge of the sample. The electrons reflected from the contact, continuing their path on the lower left edge, give rise to a chemical potential that is lower (=voltage that is higher) than μ_L (V_L) on that edge.

B. Two quantum point contacts

Looking back at Figs. 1 and 2, another interesting interference effect is taking place which has not been observed in the experiment. When the branches of electron flow hit the upper and lower border of the sample (in the regions from 0 to $200a$ and from $800a$ to $1000a$ on both figures), there are clear interference fringes visible, perpendicular to the border. The wavelength of these fringes is larger than that of the fringes observed in the scatterer experiment (which resulted from back-and-forth scattering between the tip and the QPC). This interference pattern can be explained as a crossing of two or more coherent electron beams (branches). In Fig. 4, a simulation is shown where the current density due to two crossing Gaussian beams with wave vectors $\mathbf{k_1}$ and $\mathbf{k_2}$ is calculated. A clear interference pattern is visible, extending

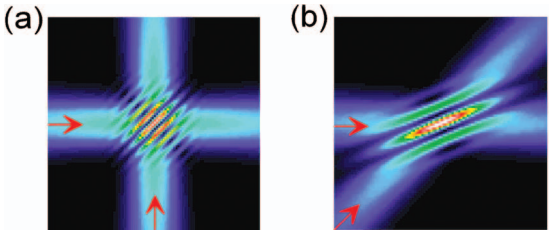

FIG. 4. (Color) Interference between two crossing Gaussian beams. The wavelength of the interference pattern depends on the angle between the beams. Fringes are more closely spaced for an angle of $\pi/2$ (a) than for an angle $\pi/4$ (b).

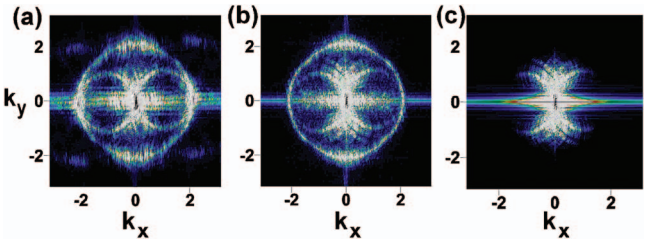

FIG. 5. (Color) Fourier transforms of the flow maps without a magnetic field: local scatterer method (a), voltage probe method (b), and current density distribution (c). Wave vectors are in units of $1/a$, the color scale has arbitrary units.

in the direction $\mathbf{k_1}$–$\mathbf{k_2}$. From comparison between Figs. 4(a) and 4(b), it is clear that the wavelength of the fringes depends on the angle between the two beams. It can be shown that this wavelength is given by

$$\Lambda = \frac{\lambda_F}{2\sin(\theta/2)}, \tag{8}$$

with $\|\mathbf{k_1}\| = \|\mathbf{k_2}\| = 2\pi/\lambda_F$, and θ the angle between the beams.

The different periodicities in the different flow maps can be made more visible by doing a Fourier transformation. In Fig. 5, this is done for columns 1 to 400 of the flow maps in Fig. 1 without a magnetic field. In both maps where an STM is used, a circle with radius $\approx 2\pi/3a$ centered on $(k_x, k_y) = (0,0)$ can be seen. This circle corresponds to the interference pattern resulting from a superposition of paths between the STM tip and the quantum point contact, which creates the fringes spaced at half the Fermi wavelength. In the current density distribution [Fig. 5(c)], this circle is, of course, absent.

Another feature in Fig. 5 is the presence of two smaller circles centered on the X axis. They result from the interference effect between crossing beams explained above. Using Eq. (8) together with the fact that the intereference pattern is directed along $\mathbf{k_1}$–$\mathbf{k_2}$, these circles can indeed be reproduced by having interference between a main beam directed along the X axis and others crossing it. While this effect has nothing to do with scattering off the STM tip, these circles are visible in Fourier transforms of all flow maps, including that of the current density distribution.

If one looks at the plot of the transport current with a magnetic field (Fig. 2), one can see that some branches bend upwards, while other bend downwards under the influence of the magnetic field. This can be interpreted as follows. In the device, the chemical potential will be somewhere between that of the left and the right lead. If one assumes that the chemical potential on the left lead is larger than that on the right, we have an excess of electrons flowing from left to right. On the other hand, we have a deficit of electrons ("holes") flowing the other way. These electrons and holes bend in opposite ways under the influence of a magnetic field, because they fill different scattering states. It is clear then that electrons and holes, and thus branches curving upwards and downwards, are emerging from different reservoirs and are thus phase incoherent. Now, at crossings between two incoherent beams, an interference pattern, such as that in Fig. 4, will not occur. As a result, one does not expect to see interference between beams with different chirality.

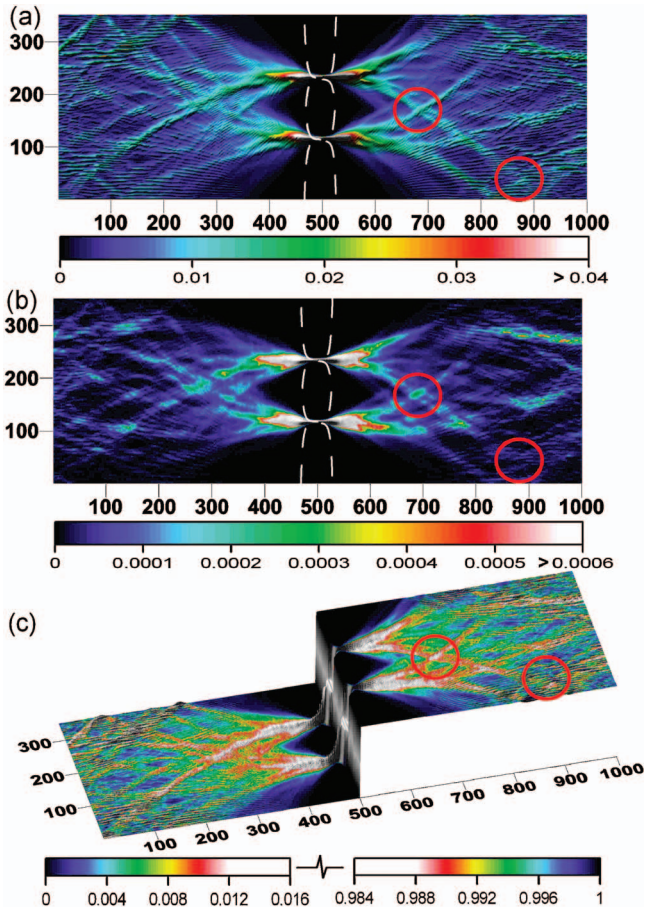

FIG. 6. (Color) Maps of electron flow through a double quantum point contact with a moderate magnetic field. Transport current density distribution (a), STM conductance map (b), and STM volt probe map (c). Units on the color scales are the same as in Fig. 1. The voltage map is symmetrized with respect to the direction of the magnetic field. In the conductance map, interference fringes with wavelength $\lambda_F/2$ resulting from scattering between the STM tip and the QPC are smoothed out.

In order to test this statement, we considered a system of two QPCs placed above each other. The potential of both QPCs has the same form as in Eq. (7), and all parameters are chosen as in Fig. 2. Results are shown in Fig. 6. Under the influence of the magnetic field, the branches are curved. One can see the interference between beams with the same chirality, but there is no interference at the crossing of two beams with opposite chirality, as we expected. This distinction becomes clear when comparing the crossings encircled in Fig. 6. To make things more clear, we have smoothed out the interference fringes in Fig. 6(b) resulting from scattering between the tip and QPC which had a wavelength of $\lambda_F/2$. In Fig. 6(c), we symmetrized the voltage probe plot with respect to the direction of the magnetic field. Also in this plot, the behavior for coherent beams crossing is different from that for incoherent branches. This proves that the effect could be studied experimentally.

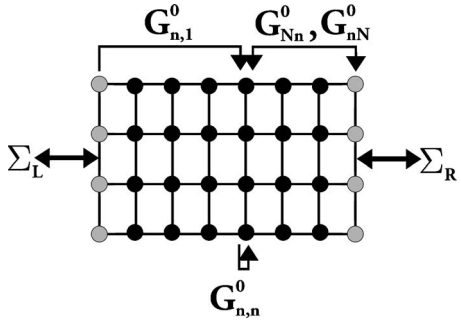

FIG. 7. Green's functions necessary to calculate the relevant quantities of our system. The first and last columns of the lattice are colored gray to indicate that they are influenced by the self-energies Σ_L and Σ_R of the leads.

V. NUMERICAL METHOD

A. Introduction

The basic quantities that need to be calculated in order to describe the scanning probe experiments are transmission coefficients from one lead to another. In Sec. V, it will be shown that these transmission coefficients, and in fact all quantities we wish to calculate (density of states, current density distribution,…) can be expressed in terms of the Green's function matrices G^0_{n1}, G^0_{nn}, G^0_{nN}, and G^0_{Nn} (for all possible values of n). These $M \times M$ matrices $G^0_{ll'}$ are defined as

$$\langle m|G^0_{ll'}|m'\rangle = \langle m,l|G^0|m',l'\rangle, \tag{9}$$

where

$$G^0 = \frac{1}{E + \mathrm{i}\,\eta - H^d - \Sigma_L - \Sigma_R} \tag{10}$$

is the Green's function of the device *without* the influence of the tip. In this expression, H^d is the Hamiltonian of the central device disconnected from the leads, while Σ_L and Σ_R are self-energies of the left and right lead, respectively. The Green's functions $G^0_{ll'}$ are thus submatrices of G^0 connecting points from column l' to those of column l of the lattice (see Fig. 7).

The method used to calculate these Green's functions will be presented in Appendix A, the main result being that they can be obtained with a number of operations that scales as M^3N. For calculation of the self-energies of the leads, we have chosen a method originally developed for the calculation of surface electronic structure, described in full detail in Refs. 17 and 18.

B. Local scatterer method

The scattering potential created by the STM tip is modeled by a delta function on a site (m,n), so it adds a repulsive contribution $V^{\mathrm{tip}} = v\,|m,n\rangle\langle m,n|$ to the Hamiltonian (4). As explained in Sec. II A, one has to calculate a conductance difference

$$\Delta g(m,n) = \frac{2e^2}{h}[T^0 - T(m,n)], \tag{11}$$

for every tip position (m,n). The transmittance $T(m,n)$ can be calculated by[1]

$$T(m,n) = \mathrm{Tr}[\Gamma_R G_{N1} \Gamma_L G^{\dagger}_{N1}], \tag{12}$$

with $\Gamma_{L(R)}$ related to the retarded self-energies $\Sigma_{L(R)}$ of the left (right) lead as

$$\Gamma_{L(R)} = \mathrm{i}(\Sigma_{L(R)} - \Sigma^{\dagger}_{L(R)}), \tag{13}$$

and G_{N1} is the Green's function between columns 1 and N. The matrix G_{N1} includes the effect of the STM tip, and is therefore different from G^0_{N1}, mentioned in the Introduction.

In Ref. 9, one uses the SRGF method for calculating G_{N1}. First, the system is divided into its separate columns (by making the hopping matrices between them zero), and the repulsive potential V^{tip} is added on a certain site. Subsequently the columns are attached one by one making use of Dyson's equation. This attachment procedure has to be started over and over again for every single position of the tip, and the method is therefore quite inefficient (scaling as M^4N^2 in the number of operations).

However, supposed that we have access to the Green's functions G^0_{n1}, G^0_{Nn}, and G^0_{nn} (see Appendix A), we can include the effect of the tip with Dyson's equation:

$$G = G^0 + G^0 V G, \tag{14}$$

where V is the potential introduced by the tip, $V = V^{\mathrm{tip}}$. Projecting (14) between columns 1 and N, one obtains [it is assumed that the tip is located at lattice site (m,n)]

$$G_{N1} = G^0_{N1} + G^0_{Nn} V^{\mathrm{tip}}_{nn} (1 - G^0_{nn} V^{\mathrm{tip}}_{nn})^{-1} G^0_{n1}. \tag{15}$$

Since V^{tip} has only one nonzero element, the inversion $(1 - G^0_{nn} V^{\mathrm{tip}}_{nn})^{-1}$ will boil down to the inversion of a scalar. This means that no extra matrix inversions are needed to find G_{N1} for an arbitrary lattice position of the tip, once we have the functions G^0_{Nn}, G^0_{nn} and G^0_{n1} for all n. In Appendix A, we will show a way of calculating these functions with a computational effort scaling like M^3N. In this way, we gain a factor MN over the SRGF method.

At first sight, it might seem that this efficiency is decreased for the complete calculation because one has to evaluate the trace in Eq. (12) for every tip position, which involves products of $M \times M$ matrices, so that the total effort for all tip positions would scale as M^4N. However, we have a better way of evaluating this trace, scaling as M^3N, so that we do not loose our efficiency. Technical details are described in Appendix B.

C. Voltage probe method

The STM tip will now be modeled by a one-dimensional (1D) lead, attached to the central device at position (m,n). The voltage on the tip can be written as a function of the transmission coefficients $T_{\mathrm{tip},L}$ and $T_{\mathrm{tip},R}$ between the STM tip and the left and right leads [Eq. (3)]. These transmittances, with the tip positioned over site (m,n), can be expressed as

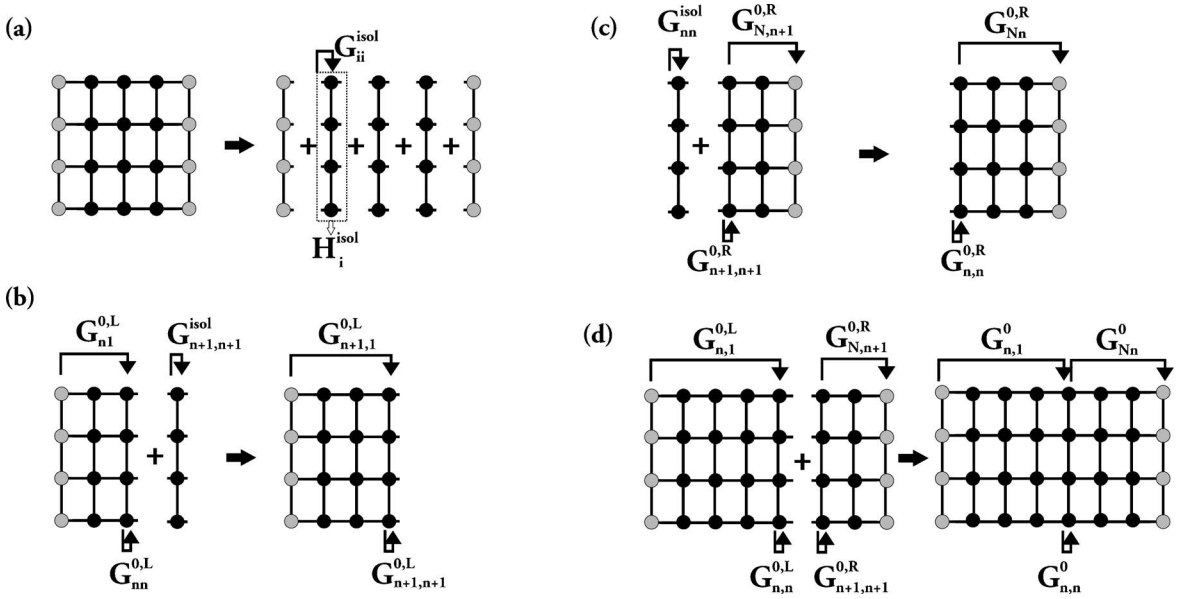

FIG. 8. Green's function method. After the hopping matrices between columns are set to zero to separate the device in vertical slices, and their Green's functions G_{ii}^{isol} are calculated (a), the slices are added one by one to obtain $G_{N1}^{0,L}$ (b). Then, the isolated slices are added to each other again but now starting from the right (c). Finally, by combining sections pairwise, one can obtain the G_{Nn}^{0}, G_{nn}^{0}, and G_{n1}^{0} (d). In the figure, the first and last column of the device are colored gray to denote the influence of the self-energies of the leads.

$$T_{\mathrm{tip},L} = \mathrm{Tr}[\Gamma_{\mathrm{tip}} G_{n1} \Gamma_L G_{n1}^{\dagger}], \tag{16a}$$

$$T_{\mathrm{tip},R} = \mathrm{Tr}[\Gamma_{\mathrm{tip}} G_{nN} \Gamma_R G_{nN}^{\dagger}], \tag{16b}$$

where $\Gamma_{\mathrm{tip}} = \mathrm{i}(\Sigma_{\mathrm{tip}} - \Sigma_{\mathrm{tip}}^{\dagger})$. Since the lead modeling the tip is one-dimensional, the self-energy Σ_{tip} is known analytically[1]

$$\Sigma_{\mathrm{tip}} = -te^{\mathrm{i}[\arccos(1-E/2t)]}. \tag{17}$$

The SRGF technique cannot be used to obtain the Green's functions G_{n1} and G_{nN} in expression (16). But we can use Dyson's equation (14) to relate them to Green's functions of the device without the tip (calculated in Appendix A)

$$G_{n1} = (1 - G_{nn}^{0} V_{nn}^{\mathrm{tip}})^{-1} G_{n1}^{0}, \tag{18a}$$

$$G_{nN} = (1 - G_{nn}^{0} V_{nn}^{\mathrm{tip}})^{-1} G_{nN}^{0}, \tag{18b}$$

where the tip influence leads to an imaginary potential $V^{\mathrm{tip}} = \Sigma_{\mathrm{tip}} |mn\rangle\langle mn|$.

Again, the inversion $(1 - G_{nn}^{0} V_{nn}^{\mathrm{tip}})^{-1}$ will reduce to the inversion of a scalar, because V^{tip} has only one nonzero element. In this case, the calculation of the traces in Eqs. (16a) and (16b) is also not computationally expensive since Γ_{tip} has only one nonzero element. Therefore the total computational effort scales like M^3N, needed for the calculation of the Green's functions without the influence of the tip (see Appendix A).

D. LDOS—electron density

It can be useful to calculate the local density of states (LDOS) and the electron density distribution in the sample (without the STM tip over the sample) for comparing them with the two imaging methods. For the LDOS, the standard expression is[1]

$$\rho(E,m,n) = -\frac{1}{\pi} \mathrm{Im}\langle m | G_{nn}^{0}(E) | m \rangle. \tag{19}$$

The electron density in the sample can then be found by integrating over energy.

E. Current density distribution

When a magnetic field is present, persistent currents are flowing through the device, even in the absence of an applied bias. In a recent paper by Cresti *et al.*,[19] an expression for this equilibrium current is derived from the Keldysh formalism. Adapted to our notation, the expression for the particle current at temperature $T=0$ flowing from one node to a neighboring node reads (remember that m labels the rows of the lattice, n the columns)

$$I_{(m,n-1)\to(m,n)}^{\mathrm{eq}} = \frac{2e}{\hbar} \int_0^{E_F} \frac{\mathrm{d}E}{2\pi} 2\,\mathrm{Re}\langle m | [G_{nn}^{0} \Sigma_n^{\mathrm{left}} - \Sigma_n^{\mathrm{left}} G_{nn}^{0}] | m \rangle, \tag{20a}$$

$$I_{(m,n)\to(m+1,n)}^{\mathrm{eq}} = \frac{2e}{\hbar} \int_0^{E_F} \frac{\mathrm{d}E}{2\pi} 2\,\mathrm{Re}\langle m+1 | [t_{m,n}^{y} (G_{nn}^{0} - G_{nn}^{0\dagger})] | m \rangle. \tag{20b}$$

Here, E_F is the Fermi energy of the device, and e is the negative electronic charge. We have also introduced

$$\Sigma_n^{\mathrm{left}} = V_{n,n-1} G_{n-1,n-1}^{0,L} V_{n-1,n}, \tag{21}$$

where $V_{n,n-1}$ describes the hopping between columns $n-1$ and n. The Green's functions $G_{nn}^{0,L}$ are defined in Fig. 8(d) of Appendix A.

It is clear, by taking the trace over the row indices m, that the total current flowing through every single column is

equal to zero, so as expected in equilibrium there will be no net current through the leads. Also, when no magnetic field is present, all Green's functions in Eqs. (20a) and (20b) are symmetric so that the equilibrium current density in this case vanishes like it should.

In the nonequilibrium situation, the applied bias leads to an additional transport current. Since persistent currents are antisymmetric with respect to the direction of the field, we can define a pure transport current as the symmetric part of the total current density distribution. This transport current is gauge invariant, and corresponds to a physically relevant (and measurable) quantity. In the linear response regime, it is given by (see also Ref. 19)

$$I_{(m,n-1)\to(m,n)} = \frac{-2e^2V}{2\pi\hbar}\{A(E)|_{+B} + A(E)|_{-B}\},$$

with

$$A(E) = 2\,\mathrm{Im}\langle m|[G^0_{nn}\Gamma^{\mathrm{right}}_n G^{0\dagger}_{nn}(\Sigma^{\mathrm{left}}_n)^\dagger]|m\rangle, \qquad (22a)$$

$$I_{(m,n)\to(m+1,n)} = \frac{-2e^2V}{2\pi\hbar}\{C(E)|_{+B} + C(E)|_{-B}\},$$

with

$$C(E) = 2\,\mathrm{Im}\langle m+1|[t^y_{m,n}G^0_{nn}\Gamma^{\mathrm{right}}_n G^{0\dagger}_{nn}]|m\rangle, \qquad (22b)$$

where $V=V_L-V_R$ is the potential difference between the leads, and

$$\Sigma^{\mathrm{left}}_n = V_{n,n-1}G^{0,L}_{n-1,n-1}V_{n-1,n}, \qquad (23a)$$

$$\Sigma^{\mathrm{right}}_n = V_{n,n+1}G^{0,R}_{n+1,n+1}V_{n+1,n}, \qquad (23b)$$

$$\Gamma^{\mathrm{right}}_n = \mathrm{i}[\Sigma^{\mathrm{right}}_n - (\Sigma^{\mathrm{right}}_n)^\dagger]. \qquad (23c)$$

The Green's functions $G^{0,L(R)}_{nn}$ in these expressions are defined in Fig. 8(d) of Appendix A.

VI. CONCLUSION

We have established an efficient tight-binding method to numerically calculate spatial maps of electron flow as obtained in a recent series of scanning probe experiments where an STM tip is used as a local scatterer for electrons.[6] The computational effort of our numerical approach scales like M^3N (in the limit $N\gg 1$), where M is the width of the lattice and N is the length. It is in this way more efficient than the standard recursive Green's function (SRGF) method which scales like M^4N^2 for the same problem.

We have also shown expressions for the local density of states, the electron density, and the current density distribution. These quantities cannot be calculated within the SRGF approach, but within our scheme they can be expressed in terms of the same Green's functions already known from the numerical simulation of the scanning probe experiment.

When a magnetic field is applied, backscattering of electrons will be strongly reduced because of the presence of edge states so that the original STM method does not give the desired results. Therefore, a probe method was proposed where the tip is used to measure the local chemical potential. The image one obtains from such a method is not always directly related to the current pattern in the sample, but one can expect to obtain relevant information about transport in the sample.

The power of the method was proven in example calculations, where a tight-binding lattice with more than 350 000 sites has been used. Moreover, by direct comparison between a numerical simulation of the experiment and a calculation of the exact current density distribution, it became clear that the original scanning probe technique of Topinka *et al.*[6] is really imaging current flow. Furthermore, an interference phenomenon has been predicted which results from the crossing of phase coherent branches, and a new setup with two QPCs has been discussed to distinguish between crossings of coherent branches and incoherent ones. This distinction is visible both when the tip is used as a scatterer and when it is used as a voltage probe, so that an experimental investigation of the effect should be possible.

It should be clear that the method proposed is very general, and the information obtained by the different imaging tools very broad so that it can be used to study electron flow in a variety of systems ranging from, e.g., the quantum Hall effect[4] to quantum chaos in electron billiards.[20] Moreover, including the spin degrees of freedom proves to be rather easy; every matrix element should be replaced by a spinor. As such, an even broader range of phenomena could be studied, ultimately also those including spin-orbit coupling (e.g., the spin Hall effect[21,22]).

APPENDIX A: CALCULATION OF GREEN'S FUNCTIONS RELEVANT TO OUR PROBLEM

In the paper, it became clear that indeed all quantities we need can be expressed in terms of a small subset of Green's functions G^0_{n1}, G^0_{nn}, G^0_{nN}, and G^0_{Nn} (see Fig. 7). In this appendix, we will treat in detail how to obtain these functions with a numerical effort that scales like M^3N.

The first step is to divide the central device into its separate columns and to put the hopping matrices between them equal to zero so that the columns become isolated, as depicted in Fig. 8(a). Next, one calculates the Green's function G^{isol}_{ii} for every isolated column $i=1,2,\cdots,N$. This first step thus needs a total of N inversions.

The next step is to attach the isolated columns one by one to each other by including the hopping matrices between them using Dyson's equation (see, e.g., Ref. 2). As such, one calculates the Green's functions $G^{0,L}_{n1}$ and $G^{0,L}_{nn}$ [see Fig. 8(b)]. Please note that since not all columns are attached to each other in $G^{0,L}_{n1}$ and $G^{0,L}_{nn}$ (only those to the left of column n), these Green's functions are not equal to the Green's functions G^0_{n1} and G^0_{nn} we are trying to obtain. The superscript L is added to make this distinction clear. Attachment of a single isolated column costs one matrix inversion, so a total of $N-1$ inversions are necessary for the second step.

For the third step, we start over from the isolated Green's functions already calculated in step 1, and glue them together by using Dyson's equation, but now beginning from the right [see Fig. 8(c)]. The Green's functions we calculate with ev-

ery step are $G^{0,R}_{Nn}$, $G^{0,R}_{nn}$, and $G^{0,R}_{nN}$. Again, a single matrix inversion is needed for the attachment of a single column, so a total of $N-1$ inversions for the completion of the third step.

The final step is to get the G^0_{Nn}, G^0_{nN}, G^0_{nn}, and G^0_{n1} we are looking for by attaching the previously calculated Green's functions in pairs, as illustrated in Fig. 8(d). One takes a section to the left with Green's functions $G^{0,L}_{n1}$ and $G^{0,L}_{nn}$, and attaches it to a section to the right with Green's functions $G^{0,R}_{N,n+1}$ and $G^{0,R}_{n+1,n+1}$. A single inversion is necessary for each pairwise addition.

In total we need $N+3(N-1)$ inversions for calculating G^0_{Nn}, G^0_{nN}, G^0_{nn}, and G^0_{n1} for all n. Computational effort for inversion of a single matrix scales like M^3, so our method scales indeed like M^3N for large N.

APPENDIX B: EVALUATION OF THE TRACE

For the scatterer method, it is necessary to calculate the conductance difference in Eq. (11). For this, it seems that we have to evaluate the trace in Eq. (12) for all MN tip positions. This trace contains products of $M\times M$ matrices, so the numerical effort for this step would scale like M^4N. As such one would loose a factor of M in efficiency compared to the rest of the calculation. However, there is a better way to evaluate the conductance difference in Eq. (11).

We write [see Eq. (15)]

$$G_{N1} = G^0_{N1} + A, \tag{B1}$$

with the $M\times M$ matrix,

$$A = G^0_{Nn} V^{\mathrm{tip}}_{nn} (1 - G^0_{nn} V^{\mathrm{tip}}_{nn})^{-1} G^0_{n1}. \tag{B2}$$

It is important now to make it clear that since V^{tip}_{nn} has only one nonzero element, namely on position (m,m), one can write A as a product of a column matrix and a row matrix,

$$A = [G^0_{Nn}]_{m\text{th column}} \tau [G^0_{n1}]_{m\text{th row}}, \tag{B3}$$

with the scalar τ given by (v is the magnitude of the repulsive tip potential)

$$\tau = \frac{v}{1 - v\langle m|G^0_{nn}|m\rangle}. \tag{B4}$$

By substituting Eq. (B1) into Eq. (12), one obtains

$$T(m,n) = T^0 + 2\,\mathrm{Re}\,\mathrm{Tr}[\Gamma_R A \Gamma_L (G^0_{N1})^\dagger] + \mathrm{Tr}[\Gamma_R A \Gamma_L A^\dagger].$$

In order to evaluate the conductance difference $\Delta g(m,n)$, we need to evaluate only the last two terms. The last term only involves products of an $M\times M$ matrix with row or column matrices because of the special form of A. The computational effort for this term scales thus as M^2, which corresponds to a total effort of M^3N for all tip locations. Now, since the product $\Gamma_L(G^0_{N1})^\dagger$ is independent of the tip position, it has to be calculated only once (with an effort M^3). When this matrix is known, the trace in the second term also contains only products of an $M\times M$ matrix with a row or column matrix, so the total effort for this term also scales like M^3N in the limit of large N.

*Electronic address: georgo@mpi-halle.de
†Electronic address: bruno@mpi-halle.de
‡URL: http://www.mpi-halle.de

[1] S. Datta, *Electronic Transport in Mesoscopic Systems* (Cambridge University Press, England, 1995).
[2] D. K. Ferry and S. M. Goodnick, *Transport in Nanostructures* (Cambridge University Press, England, 1997).
[3] B. J. van Wees, H. van Houten, C. W. J. Beenakker, J. G. Williamson, L. P. Kouwenhoven, D. van der Marel, and C. T. Foxon, Phys. Rev. Lett. **60**, 848 (1988); D. A. Wharam, T. J. Thornton, R. Newbury, M. Pepper, H. Ahmed, J. E. F. Frost, D. G. Hasko, D. C. Peacock, D. A. Ritchie, and G. A. C. Jones, J. Phys. C **21**, L209 (1988).
[4] K. von Klitzing, G. Dorda, and M. Pepper, Phys. Rev. Lett. **45**, 494 (1980).
[5] P. A. Lee, A. D. Stone, and H. Fukuyama, Phys. Rev. B **35**, 1039 (1987).
[6] M. A. Topinka, B. J. LeRoy, S. E. J. Shaw, E. J. Heller, R. M. Westervelt, K. D. Maranowski, and A. C. Gossard, Science **289**, 2323 (2000).
[7] M. A. Topinka, B. J. LeRoy, R. M. Westervelt, S. E. J. Shaw, R. Fleischmann, E. J. Heller, K. D. Maranowski, and A. C. Gossard, Nature (London) **410**, 183 (2001).
[8] B. J. LeRoy, J. Phys.: Condens. Matter **15**, R1835 (2003).
[9] G.-P. He, S.-L. Zhu, and Z. D. Wang, Phys. Rev. B **65**, 205321 (2002).
[10] M. Büttiker, Phys. Rev. Lett. **57**, 1761 (1986).
[11] M. Büttiker, Phys. Rev. B **38**, 9375 (1988).
[12] P. Muralt and D. W. Pohl, Appl. Phys. Lett. **48**, 514 (1986).
[13] J. R. Kirtley, S. Washburn, and M. J. Brady, Phys. Rev. Lett. **60**, 1546 (1988).
[14] R. E. Peierls, Z. Phys. **80**, 763 (1933).
[15] J. H. Davies, *The Physics of Low-Dimensional Semiconductors: An Introduction* (Cambridge University Press, Cambridge, 1998).
[16] M. Büttiker, Phys. Rev. B **40**, R3409 (1989).
[17] M. P. Lopéz Sancho, J. M. Lopéz Sancho, and J. Rubio, J. Phys. F: Met. Phys. **15**, 851 (1985).
[18] I. Turek, V. Drchal, J. Kudrnovský, M. Šob, and P. Weinberger, *Electronic Structure of Disordered Alloys, Surfaces and Interfaces* (Kluwer, Boston, 1997).
[19] A. Cresti, R. Farchioni, G. Grosso, and G. P. Parravicini, Phys. Rev. B **68**, 075306 (2003).
[20] C. M. Marcus, A. J. Rimberg, R. M. Westervelt, P. F. Hopkins, and A. C. Gossard, Phys. Rev. Lett. **69**, 506 (1992).
[21] J. E. Hirsch, Phys. Rev. Lett. **83**, 1834 (1999).
[22] J. Sinova, D. Culcer, Q. Niu, N. A. Sinitsyn, T. Jungwirth, and A. H. MacDonald, Phys. Rev. Lett. **92**, 126603 (2004).